

9-16-2013

Nanopore surface coating delivers nanopore size and shape through conductance-based sizing

Cameron M. Frament
University of Rhode Island

Y. M. Nuwan D.Y. Bandara
University of Rhode Island

Jason R. Dwyer
University of Rhode Island, jason_dwyer@uri.edu

Follow this and additional works at: https://digitalcommons.uri.edu/chm_facpubs

Citation/Publisher Attribution

Frament, C. M., Bandara N., & Dwyer, J. R. (2013). Nanopore surface coating delivers nanopore size and shape through conductance-based sizing. *ACS Appl. Mater. Interfaces*, 5(19), 9330-9337. doi: 10.1021/am4026455

Available: <http://dx.doi.org/10.1021/am4026455>

This Article is brought to you by the University of Rhode Island. It has been accepted for inclusion in Chemistry Faculty Publications by an authorized administrator of DigitalCommons@URI. For more information, please contact digitalcommons-group@uri.edu. For permission to reuse copyrighted content, contact the author directly.

Nanopore surface coating delivers nanopore size and shape through conductance-based sizing

The University of Rhode Island Faculty have made this article openly available.
Please let us know how Open Access to this research benefits you.

This is a pre-publication author manuscript of the final, published article.

Terms of Use

This article is made available under the terms and conditions applicable towards Open Access Policy Articles, as set forth in our [Terms of Use](#).

Nanopore surface coating delivers nanopore size and shape through conductance-based sizing.

*Cameron M. Frament, Nuwan Bandara and Jason R. Dwyer**

Article published in final form at

ACS Appl. Mater. Interfaces, 2013, 5 (19), pp 9330–9337

DOI: 10.1021/am4026455 <https://pubs.acs.org/doi/pdf/10.1021/am4026455>

Supporting Information Available Free of Charge at:

<https://pubs.acs.org/doi/suppl/10.1021/am4026455>

Nanopore surface coating delivers nanopore size and shape through conductance-based sizing.

*Cameron M. Frament, Nuwan Bandara and Jason R. Dwyer**

Department of Chemistry, University of Rhode Island, 51 Lower College Rd., Kingston, Rhode Island, 02881, United States

KEYWORDS. Electric double layer, nanopore surface charge, nanopore conductance, nanopore shape, silicon nitride nanopore, silicon oxide nanopore, biomimetic nanopore, single-molecule sensing.

ABSTRACT. The performance of nanopore single-molecule sensing elements depends intimately on their physical dimensions and surface chemical properties. These factors underpin the dependence of the nanopore ionic conductance on electrolyte concentration, yet the measured, or modeled, dependence only partially illuminates the details of geometry and surface chemistry. Using the electrolyte-dependent conductance data before and after selective surface functionalization of solid-state nanopores, however, introduces more degrees of freedom and improves the performance of conductance-based nanopore characterizations. Sets of representative nanopore profiles were used to generate conductance data, and the nanopore shape and exact dimensions were identified, through conductance alone, by orders-of-magnitude

reductions in the geometry optimization metrics. The optimization framework could similarly be used to evaluate the nanopore surface coating thickness.

Introduction

Nanopores are the core element of a powerful new class of methods and devices for single-molecule sensing and manipulation¹⁻⁹. A nanopore, at its most basic level, is a nanometer-diameter through-hole in an insulating membrane. When such a membrane is used to divide an electrolyte-filled cell, and a transmembrane potential is applied, the flow of electrolyte ions through the nanopore can be readily measured. The presence of a single molecule in the nanopore can then be detected and identified if it perturbs the electrolyte-only, open pore current in a characteristic way. Experimental measurements of nanopore conductance in the absence of analyte show a rich behavior dependent upon the intricate interplay between nanopore geometry, nanopore surface chemistry, electrolyte composition and potential drop across the nanopore. This behavior is captured by theoretical treatments and simulations employing varying levels of sophistication¹⁰⁻¹⁶.

There are three broad classes of nanopores in routine use: proteinaceous pores such as α -hemolysin and MSPA, solid-state pores such as those fabricated in silicon nitride and silicon oxide using direct electron- and ion-beam milling, and solid-state pores formed by solution processing of ion-tracked polymer and silicon nitride films^{1-4, 7, 17}. These pore classes and fabrication conditions present quite different geometries and surface chemistries, and quite different challenges and opportunities. Protein pores offer self-assembly of reproducible pore structures with rich surface chemistries determined by the functional groups—amino acids in native pore structures, modifiable through complex formation and biochemical manipulation—

lining the nanopore interior. Solid-state nanopores crafted in micro-and nanofabrication-compatible materials such as silicon nitride and silicon dioxide offer the prospect of streamlined fabrication of robust, complex nanopore devices for single molecule measurement and manipulation. The ability to create solid-state nanopores with a variety of sizes and shapes to accommodate a wide range of target applications is also driving their increasing popularity. The surface chemistry of native solid-state nanopores is relatively simple, with silicon oxide nanopore surface chemistry, for instance, typically treated as being governed by the single chemical equilibrium¹⁰⁻¹¹



Advances in the surface chemical modification of nanopores, however, are dramatically blurring the boundaries between the rich surface chemistry of protein pores and the relatively straightforward chemistry of native solid-state pores. A variety of methods exists to tune nanopore surface chemistry, from direct covalent attachment to the use of physi- and chemisorbed layers¹⁸⁻²². Such surface modifications can be used to alter the nanopore surface chemistry and they can also be used to appreciably change the physical dimensions of the nanopore. Thus, what emerges is a design framework in which physical and molecular approaches can be used to tune the solid-state nanopore size and properties to suit applications as diverse as the fundamental investigation of receptor-ligand interactions²³ and rapid, low-cost DNA sequencing²⁴. The consequent challenge is the characterization of the resulting nanopore on a length scale that is challenging to access experimentally. Characterization approaches that rely on charged particle imaging place substantial demands on the user, and require access to facilities and expertise in methods beyond those required for nanopore use^{10, 25-26}. The development of characterization methods requiring routine nanopore operation, alone, thus

continues, with the improved accessibility and efficiency of nanopore methods an attractive target^{10, 27}. Such methods would additionally promise benefits for advancing the foundations of nanopore technology by permitting, for example, nanopore size and shape to be monitored and used for feedback during solution-based nanopore fabrication approaches^{19, 28-30}.

Given the central role of the nanopore ionic conductance in many nanopore experiments, and given that the conductance is determined by factors including the nanopore size and surface chemistry, it is common to use the ionic conductance to characterize the nanopore. Using a simple but experimentally supported model for nanopore conductance^{10-11, 19}, we have previously shown that the electrolyte-dependence of the conductance offers, in general, only a limited view of nanopore structure²⁷. In particular, the ability to determine at most two nanopore geometry parameters does not necessarily permit unambiguous identification, by conductance, of nanopore shape. Independent knowledge of some elements of the size or shape, though, can be used within that framework to allow the evaluation of conductance-derived parameters, or to impose constraints that allow the partial recovery of more geometric information from nanopores described by more than two geometric parameters²⁷. In this work, we show that by using the electrolyte-dependence of nanopore conductance before and after surface coating, we can more completely characterize nanopore size and shape without the need for independent geometry inputs. In particular, for experimentally realistic three-parameter pores, the augmented approach allows nanopore size and shape to be completely recovered from the conductance.

Theory

We adopt a widely-used theoretical model for the nanopore conductance that has been successfully used to model experimental results^{10-11, 19}. We focus on nanopores less than 20nm in

diameter, for which the access resistance is a negligible contribution³¹, leaving two contributions to the nanopore conductance, $G^{10,27}$

$$G_{\text{total}} = G_{\text{bulk}} + G_{\text{surface}} \quad (2)$$

The bulk term, G_{bulk} arises from the flow of ions through the pore, treated here as a uniform flow³²

$$G_{\text{bulk}} = K \left(\int \frac{dz}{\pi(r(z))^2} \right)^{-1} = K \cdot A \quad (3)$$

where K is the solution conductivity and $r(z)$ is the radius of the pore as a function of the distance into the pore, in a cylindrical coordinate system. The surface term, G_{surface} , accounts for the flow of counterions along the charged surface of the pore, which is especially significant in low bulk ionic strength solutions¹⁰⁻¹¹

$$G_{\text{surface}} = \mu|\sigma| \left(\int \frac{dz}{2\pi r(z)} \right)^{-1} = \mu|\sigma| \cdot B \quad (4)$$

where σ is the surface charge concentration, and μ is the mobility of the counter ions proximal to the surface. This surface term thus augments the conductance with additional information involving the geometry and the surface chemistry. For a nanopore with surface chemistry governed by the chemical equilibrium in equation 1, the surface charge will arise from the charged SiO^- groups on the surface, and the mobile counterions will be cations. By solving for the equilibrium concentration of H^+ ions at the surface, $[\text{H}^+]_0$, and applying the Nernst equation³³

$$[\text{H}^+]_0 = [\text{H}^+]_{\text{bulk}} \exp(-e\beta\psi_0) \quad (5)$$

where $[\text{H}^+]_{\text{bulk}} = 10^{-\text{pH}}$, one can obtain an expression for the diffuse layer potential proximal to a negatively charged surface³³

$$\psi_D(\sigma) = \frac{1}{\beta e} \ln \frac{-\sigma}{e\Gamma + \sigma} - (\text{pH} - \text{pK}_a) \frac{\ln 10}{\beta e} - \frac{\sigma}{C} \quad (6)$$

where e is the elementary charge, $1/\beta$ is the thermal energy (at 298K for all calculations), Γ is the total surface density of surface chargeable groups, pK_a is the acid dissociation constant for equation 1, pH is the bulk solution pH , C is the Stern layer capacitance, and σ is the surface charge density. Surface functionalization likely changes the pK_a , and if the surface becomes cationic, the argument of the first logarithm becomes $(e\Gamma - \sigma)/\sigma$, and the mobile surface counterions are anions. Coupling the appropriate expression for the diffuse layer potential with the Grahame equation³³

$$\sigma(\psi_D) = \frac{2\epsilon\epsilon_0\kappa}{\beta e} \sinh\left(\frac{\beta e \psi_D}{2}\right) \quad (7)$$

where $\epsilon\epsilon_0$ is the permittivity of the solution and κ^{-1} is the Debye screening length, calculated from $\kappa^2 = \beta e^2 n_{\text{KCl}}/\epsilon\epsilon_0$ where n_{KCl} is the numerical concentration of the potassium chloride electrolyte, allows one to find a solution for the surface charge concentration of the pore^{10-11, 33}.

The nanopore conductance in equation 2 can be expressed in a form that clarifies its geometrical and surface chemical underpinnings²⁷

$$G_{\text{total}} = A K + B \mu |\sigma| \quad (8)$$

where A and B are the volume and surface integrals, respectively, in equations 3 and 4. When a continuous coating of thickness δ is applied to the nanopore surface, the new conductance of the nanopore can be expressed as

$$G'_{\text{total}}(\delta) = A'(\delta) K + B'(\delta) \mu' |\sigma'| \quad (9)$$

where the prime denotes the parameter value after surface coating. Measurement of the nanopore conductance at a minimum of two electrolyte concentrations, each, before and after changing the surface coating (a dimension change, $\delta \neq 0$, is required, and a surface charge density change from σ to σ' is likely), formally allows for the unique determination of the geometry parameters A , $A'(\delta)$, B and $B'(\delta)$. These parameters can then be used to determine the values of the underlying geometric parameters such as the nanopore limiting radius.

The implementation of this approach is not restricted to experiments in which only changes in the solution electrolyte concentration are used to predictably change the solution conductivity, K , and the surface conductivities $\mu|\sigma|$ and $\mu'|\sigma'|$. Chemical and physical parameters both implicit and explicit in Equations (6) and (7) can be used instead, including: a direct change of solution pH, a change of solvent to drive changes in ion mobility or surface acid dissociation constants, or a change in temperature to affect the surface acid dissociations and ion mobilities. The method is quite general and relies only upon the explicit functional dependence of the conductance shown in Equations (8) and (9). It does not rely upon the particular chemical or physical parameter used experimentally to deliver the underlying functional dependence of K , $\mu|\sigma|$ and $\mu'|\sigma'|$.

Methods

In all calculations where the parameters appear, the bulk solution pH was fixed at 7.5 and the nanopore membrane thickness, L , was held fixed at 30nm. The aqueous electrolyte solution was composed of potassium chloride, so that the solution conductivity was calculated from

$$K = e n_{\text{KCl}}(\mu_{\text{K}} + \mu_{\text{Cl}}) \quad (10)$$

where $\mu_K = 7.6 \times 10^{-8} \text{m}^2/(\text{V} \cdot \text{s})$ and $\mu_{\text{Cl}} = 7.9 \times 10^{-8} \text{m}^2/(\text{V} \cdot \text{s})$ are the mobilities of the potassium and chloride ions, respectively¹¹. The solution permittivity was approximated as $\epsilon\epsilon_0 = 77.75\epsilon_0$ throughout. Native, uncoated nanopores had their surface chemistry described by the equilibrium in Equation 1, with a constant $\text{pK}_a=7.9$ ³⁴. The surface charge density, σ , of the uncoated nanopores was calculated as the simultaneous solution to equations 6 and 7, where Γ and C were held constant at $8 \times 10^{18} \text{m}^{-2}$, and $0.3 \text{F} \cdot \text{m}^{-2}$, respectively, and were not changed after surface coating³³⁻³⁴.

We selected a number of common nanopore radial profiles, listed in Table 1, to describe the shape of the nanopores. We chose to model an amine-terminated, covalently modified nanopore surface to give a surface coating involving the acid-base equilibrium



and described by $\text{pK}_a = 10.8$. The 1.7nm-thick coating was assumed to smoothly and uniformly coat the surface without changing the nanopore shape and with the monolayer chains orthogonal to the surface at the point of attachment. The surface coating did, however, change the sign of the charge on the nanopore surface and the identity of the mobile surface counterions, from cations in the native pore to anions in the coated pore.

To investigate the ability of the proposed method to recover the nanopore size and shape for nanopores with limiting radii, r_0 , between 2.5 and 10nm, we computed the integrals A , $A'(\delta)$, B and $B'(\delta)$, using $\delta = 1.7\text{nm}$ to account for the length of the silane-coupled monolayer, for each nanopore radial profile listed in Table 1. The lower limit was chosen to prevent the monolayer from sterically closing the pore, but must in practice be responsive to the onset of overlapping Debye layers. To generate the set of reference (ref) values, we varied the limiting

radii, $r_{0,\text{ref}}$, and fixed the inner cylinder lengths, l_{ref} of the exponential-cylindrical and conical cylindrical models at 11 nm, the slope parameter b_{ref} of the exponential-cylindrical model at 0.19nm^{-1} , and the outer radii, R_{ref} of the hyperbolic, conical and conical-cylindrical models at $r_{0,\text{ref}} + 10\text{nm}$ ^{10, 27, 31}. We then used these reference calculations to geometry-optimize all of the radial profiles at each limiting radius. For example, an $r_{0,\text{ref}} = 3\text{nm}$ exponential-cylindrical nanopore was used to geometry-optimize cylindrical, conical, hyperbolic, conical-cylindrical and exponential-cylindrical profiles, and an $r_{0,\text{ref}} = 7\text{nm}$ cylindrical nanopore was used to geometry-optimize cylindrical, conical, hyperbolic, conical-cylindrical and exponential-cylindrical profiles. All native geometry parameters, except for L , were varied during the geometry optimizations. The geometry optimizations were first performed with fixed monolayer thickness, $\delta = 1.7\text{nm}$, and then repeated in a separate trial with δ as a free parameter, in an attempt to recover the layer thickness. The optimization used the Nelder-Mead minimization algorithm, and involved varying the underlying geometry parameters (e.g. r_0 , l , etc.) of the radial profiles to minimize

$$\text{RMSE}_{\text{AB}} = \sqrt{\frac{1}{4} \left(\left(\frac{A_{\text{fit}} - A_{\text{ref}}}{A_{\text{ref}}} \right)^2 + \left(\frac{B_{\text{fit}} - B_{\text{ref}}}{B_{\text{ref}}} \right)^2 + \left(\frac{A'_{\text{fit}} - A'_{\text{ref}}}{A'_{\text{ref}}} \right)^2 + \left(\frac{B'_{\text{fit}} - B'_{\text{ref}}}{B'_{\text{ref}}} \right)^2 \right)} \quad (12)$$

where the subscript ‘‘ref’’ denotes the known, reference, parameter value, and the subscript ‘‘fit’’ denotes the corresponding value calculated using the trial values. Given the form of the conductance (equations 8 and 9), minimization of RMSE_{AB} delivers a weighted conductance-based geometry optimization. An error threshold of 10^{-12} was used in the optimization runs, and the optimized structure was the result of the trial with the lowest RMSE_{AB} . A similar metric expressed directly in terms of conductance requires an average across N potassium chloride concentrations

$$\text{RMSE}_G = \sqrt{\frac{1}{N} \sum_{[\text{KCl}]} \frac{1}{2} \left(\left(\frac{G_{\text{fit}}([\text{KCl}]) - G_{\text{ref}}([\text{KCl}])}{G_{\text{ref}}([\text{KCl}])} \right)^2 + \left(\frac{G'_{\text{fit}}([\text{KCl}]) - G'_{\text{ref}}([\text{KCl}])}{G'_{\text{ref}}([\text{KCl}])} \right)^2 \right)} \quad (13)$$

The potassium chloride concentrations used here ranged from 0.01M to 1M, with the i -th concentration calculated from $10^{-2+(i-1)0.01}\text{M}$.

Results and Discussion

In the most common implementation of conductance-based nanopore sizing, the nanopore conductance at a single electrolyte concentration is used to extract a radius, and nanopore surface charges may be either included or neglected in the calculation. We explore this canonical single-point approach as a prelude to the consideration of the more involved process outlined in the Methods section. The use of a single conductance value for geometry optimization permits only the use of single-parameter profiles—either those that are inherently single-parameter, such as the cylindrical profile, or those in which all parameters but one are fixed to particular values or fixed by functional relationships that are either known or are assumed reasonable. In addition to this strictly geometric limitation, the use of a single conductance value, G_{total} , does not allow the separation of bulk and surface contributions to the conductance. Measurement in high ionic strength solutions, though, can minimize the effect of the surface term, albeit at the cost of information about the surface chemistry. Geometry optimization of a particular nanopore profile can produce dramatically different nanopore sizes when geometry parameters that satisfy Equation 8 are determined by either including or neglecting the surface charge. These single-point geometry optimizations produce exact agreement with the reference conductance, so that no error metrics exist to evaluate the suitability of the assumed nanopore shape. Figure 1 and the

discussion that follows put the necessity to consider size, shape, surface chemistry and electrolyte composition in concert into relief.

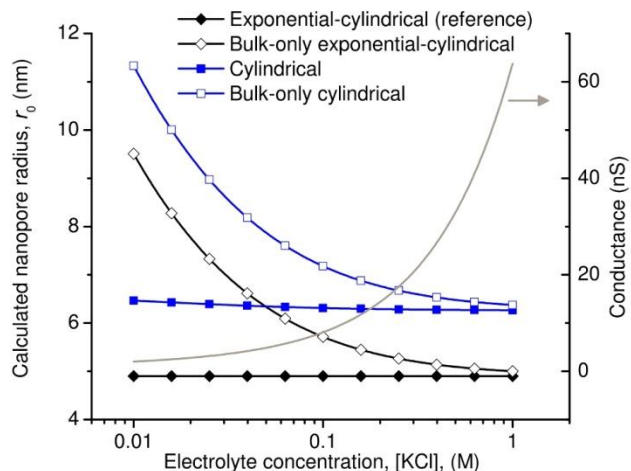


Figure 1. The conductance of an uncoated, surface-charged exponential cylindrical reference pore ($r_{0,\text{ref}} = 4.9 \text{ nm}$, $l_{\text{ref}}=11\text{nm}$, and $b_{\text{ref}}=0.19\text{nm}^{-1}$) was calculated at a number of different electrolyte concentrations. All of the plotted radii were calculated by using the single reference conductance at each electrolyte concentration to geometry optimize either the known reference radial profile (with fixed $l=11\text{nm}$, and $b=0.19\text{nm}^{-1}$), or the canonical cylindrical approximation. For each nanopore shape, the radial optimization was performed with the surface charge included and then neglected.

To generate Figure 1, the conductance of the uncoated reference nanopore was calculated using a realistic radial profile with three tunable geometric parameters (exponential-cylindrical, see Supplemental Table S1)¹⁰ and accounting for the surface charge established by the equilibrium described in Equation 1. At each electrolyte concentration considered, the single conductance value was used to determine the radius of a particular single-free-parameter nanopore profile—here, either the original reference profile with fixed $l=11\text{nm}$, and $b=0.19\text{nm}^{-1}$, or a cylindrical profile—by including or neglecting the surface charge. In solutions with high bulk conductivity

and high ionic strength, omission of the surface charge had little effect on the best-fit nanopore radii. There was, however, a clear difference in the nanopore radii determined via assumption of the nanopore shape—a difference that persisted across solution electrolyte concentrations. At lower electrolyte concentrations, the profile-specific errors in best-fit radii were dramatically superseded by the errors arising from the neglect of surface charges in the geometry optimization. This tremendous sensitivity to the surface chemistry points both to the potential to profile the surface chemistry via conductance and to the necessity to consider it^{10-11, 14, 35}. It is moreover essential to emphasize that in addition to the visible differences in cylindrical and exponential-cylindrical best-fit radii shown in Figure 1, the two optimized versions of the same nanopore have dramatically different shapes—one has a cylindrical restriction of 11 nm in length that then opens towards the membrane surfaces, the other a cylindrical restriction that spans the entire 30 nm membrane thickness. These observations underscore the importance—and difficulty—of using conductance to determine nanopore shape and surface chemistry, together: a single conductance value can be exactly satisfied by nanopores of a host of different sizes and shapes. Extension of this basic, single-point optimization to use the electrolyte-dependence of the conductance—at minimum a two-point optimization, but more practically requiring more than two data points to improve the fit statistics—offers the possibility of determining the bulk and surface contributions. In addition, the extension delivers an additional degree of freedom for nanopore geometry optimizations: it permits the optimization of radial profiles with up to two free geometry parameters²⁷. Given that transmission electron microscope (TEM)-fabricated nanopore profiles can require description by no less than three free parameters, such a geometry optimization requires parameter constraints or reductions. This has the consequence of compromising the nanopore size determination and moreover prevents even the shape of pores

from being determined without additional information²⁷. One of the substantial and myriad benefits conferred by coating nanopores with overlayers, then, is the additional degrees of freedom provided for conductance-based geometry optimizations.

Nanopores and nanopore surface functionalization are frequently characterized using a conductance-based method that does not involve variation of the electrolyte concentration, however. The approach is analogous to the single-point optimization of Figure 1 and uses the nanopore conductance at a single electrolyte concentration, before and after surface coating. The use of two conductance values provides a much-needed additional degree of freedom compared to the single-point measurement, but the available information is still limited. In particular, one would perform a single measurement of the conductance before and after (') coating, $G_1 = A K_1 + B \mu_1 |\sigma_1|$ and $G'_1(\delta) = A(\delta) K_1 + B(\delta) \mu_1' |\sigma_1'|$, respectively, where the subscript "1" denotes the particular value of the parameter. Rewriting $A(\delta) = \alpha(\delta)A$ and $B(\delta) = \beta(\delta)B$ (with different values of $\alpha(\delta)$ and $\beta(\delta)$ for each nanopore size and shape), and defining effective (eff) values $\alpha(\delta)K_1 = K_{1,\text{eff}}$ and $\beta(\delta)\mu_1' |\sigma_1'| = (\mu_1' |\sigma_1'|)_{\text{eff}}$ yields two equations $G_1 = A K_1 + B \mu_1 |\sigma_1|$ and $G'_1(\delta) = A K_{1,\text{eff}} + B (\mu_1' |\sigma_1'|)_{\text{eff}}$ that makes this approach formally equivalent to the two-point nanopore geometry optimization that had previously been explored in detail²⁷. While delivering generally superior performance to a single-point optimization, it nevertheless has well-characterized performance limitations in comparison to the optimization method introduced here. For example, such a two-point approach cannot be used to uniquely geometry optimize nanopores requiring more than two free geometry parameters²⁷.

We now consider the nanopore optimization method outlined in the Theory and Methods sections, a method that requires knowledge of the nanopore conductance at a minimum of two

electrolyte concentrations, before and after surface coating. The method therefore requires a minimum of four conductance values (a four-point optimization), but in practice more than these four conductance values would be used in order to improve the fit statistics, at least the first time that a pore was to be characterized. Equation (13) could be used to guide the geometry optimization using the conductance directly. In the conductance equations, Equations (8) and (9), however, the physical pore dimensions and the surface chemical properties are separable contributions to the conductance. To highlight the performance of the optimization method in recovering nanopore size and shape, we used Equation (12) to perform the geometry optimizations, guided by the known values of A_{ref} , $A'_{\text{ref}}(\delta)$, B_{ref} and $B'_{\text{ref}}(\delta)$. The optimization results presented here using Equation (12) deal with geometry only, and are completely independent of the surface chemistry, which need not be specified. Experimentally, this geometry-based approach would have great utility if a two-step optimization were adopted. In the first step, the conductance versus electrolyte concentration curves (Equations 8 and 9) would be fit to extract best-fit values for A , $A'(\delta)$, B and $B'(\delta)$ —parameters that would be, at this stage, devoid of physical meaning because the core geometry parameters underlying their values would not yet be considered. Within the framework of the conductance model described by Equations (8) and (9), this first step would thus require no knowledge of nanopore geometry, but would require only knowledge of its surface chemistry. Minimization of RMSE_G to achievable $\sim 10^{-12}$ levels (*cf.* Figure 2) may require slight fine-tuning of surface parameters to optimize the fit to the conductance. The best-fit A , $A'(\delta)$, B and $B'(\delta)$ would then serve as the reference values to govern the subsequent determination of nanopore size and shape using Equation (12)—a geometry-only optimization.

Figure 2 summarizes geometry optimizations, using Equation (12), selected from the full set performed. In Figure 2A, exponential-cylindrical nanopores described by three underlying geometry parameters ($r_{0,\text{ref}}$, $l=11\text{nm}$, and $b=0.19\text{nm}^{-1}$)¹⁰ were used to calculate the reference A , $A'(\delta)$, B and $B'(\delta)$. Geometry optimizations of all the radial profiles listed in Table 1 were performed, without constraints on the values of the geometry parameters (other than $L=30\text{nm}$ and $\delta = 1.7\text{nm}$, as outlined in Methods). The lowest values of the optimization metric RMSE_{AB} were for the exponential-cylindrical profile—the shape matching the reference nanopore shape—and were orders of magnitude lower, for all nanopore sizes considered, than the RMSE_{AB} for all of the other candidate nanopore shapes. The RMSE_{AB} metric was therefore clearly able to correctly identify the nanopore shape. The errors in conductance, RMSE_{G} , corresponding to all of the RMSE_{AB} -best-fit geometries, were also calculated, although they were not used for the optimization. While the RMSE_{G} are scaled by the solution and surface physicochemical parameters, they still showed the same relative trends and magnitudes as the RMSE_{AB} and the same performance in correctly identifying the nanopore shape from amongst the candidates. An examination of the best-fit limiting radii, r_0 , for each trial shape further emphasizes the merits of this conductance-based characterization approach. The cylindrical, conical and hyperbolic profiles rejected by the RMSE_{AB} metric yielded radii whose deviations from the reference radii were significant on the length scale of nanopore-based single-molecule sensing and manipulation. In spite of broad structural similarities (inner cylinders that widen towards the membrane surfaces) and limiting radii in very close agreement, the RMSE_{AB} metric was able to clearly differentiate between conical-cylindrical and exponential-cylindrical pore shapes. This inability of the conical-cylindrical pore to match the exponential-cylindrical nanopore conductance occurred in spite of the variation of $R - r_0$ from $\sim 3.5\text{nm}$ to $\sim 7\text{nm}$ with increasing

$r_{0,\text{ref}}$, and l varying from 9.8 to 11 nm versus the constant 11 nm in the reference nanopores (not shown). This ability to distinguish between even structurally similar three-parameter (or fewer) nanopore shapes using the present four-point method is in marked contrast to earlier reports using two-point conductance optimizations²⁷.

Figure 2B presents the results of the geometry optimizations of conical reference nanopores. Comparison of the RMSE_{AB} and RMSE_{G} for all best-fit trial profiles indicated, by several orders of magnitude difference in errors, that the reference nanopores were conical, and the best-fit radii r_0 and R for the conical trial profile matched the known reference values. Reassuringly, the greater parameter flexibility of the exponential-cylindrical and conical-cylindrical profiles (three parameters versus the two parameters of the conical model) could not overcome the large gap in RMSE_{AB} . The inability of the conical-cylindrical trial profile to match the conical reference conductances arises from its limiting behavior as $l \rightarrow 0$: the uncoated pore profile reduces to a conical profile, but the coated profile remains conical-cylindrical. Nevertheless, the optimized values of the conical-cylindrical profiles indicated strong conical character: limiting radii essentially matching conical reference limiting radii, and values of l nearing zero (not shown).

Four-point optimizations of hyperbolic and conical-cylindrical reference nanopores similarly allowed the correct determination of the reference nanopore shapes and their geometry parameters. A particularly interesting case of the ability of the four-point optimization to correctly determine the shape of reference nanopores with three free parameters or less occurred when using a cylindrical reference nanopore. All of the trial profiles listed in Table 1 and Supplemental Table S1 will reduce to a cylinder as a limiting case. It is therefore possible to fit a

cylindrical reference pore with a conical-cylindrical profile, for example, by satisfying either $R = r_0$, and $l = L$. It is necessary, therefore, to examine not only the $RMSE_{AB}$ or $RMSE_G$ for a particular trial profile, but also the resulting best-fit geometry parameters that could indicate a cylindrical reference nanopore even when using a conical-cylindrical trial, for example.

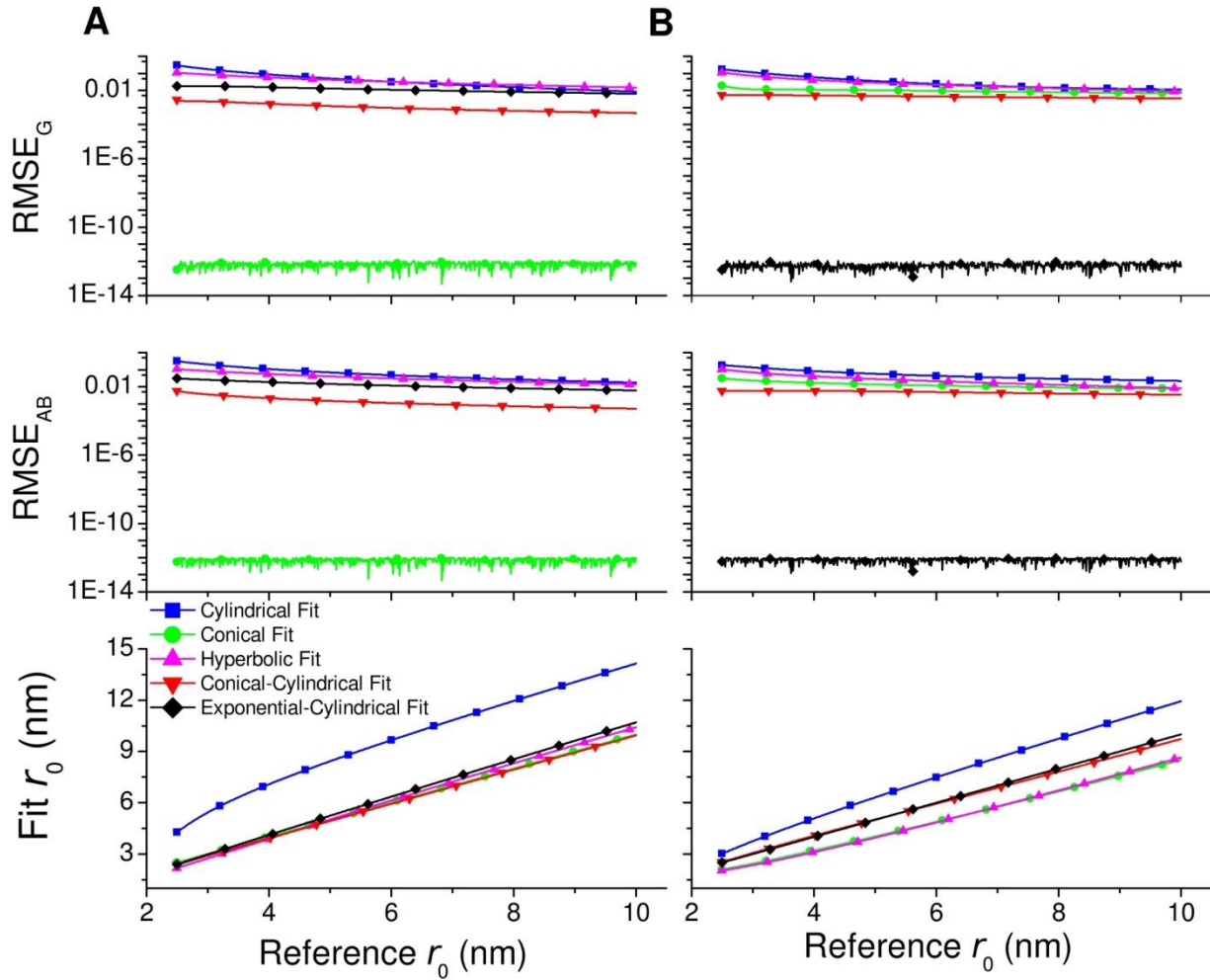


Figure 2. (A) The electrolyte-dependence of the conductance of uncoated and amine-surface-decorated exponential-cylindrical nanopores ($r_{0,ref}$, $l = 11\text{nm}$, and $b = 0.19\text{nm}^{-1}$, $\delta = 1.7\text{nm}$) was used to geometry optimize, with fixed $\delta = 1.7\text{nm}$, the nanopore profiles in Table 1 using Equation 12. Upper panels denote the error in the conductance calculated after optimization

using RMSE_{AB} , shown in the middle panel. The lower panels denote the final limiting radius of the pore for each trial profile. (B) The reference nanopore was conical with $R_{\text{ref}} = r_{0,\text{ref}} + 10\text{nm}$, and also had $\delta = 1.7\text{nm}$.

The trial nanopore profiles span a range of experimentally representative nanopore shapes and, with a maximum of only three free geometry parameters, can nevertheless reproduce experimental conductance measurements^{10, 27}. The ease with which RMSE_{AB} and RMSE_{G} , when coupled with examination of the resulting best-fit parameters, determined the optimal radial profiles with fixed- δ hinged on the number of free parameters in the trial shapes compared to the degrees of freedom delivered by the functional form of the conductance. The four-point method should also be able to uniquely geometry-optimize four-parameter models, thereby allowing the nanopore surface coating thickness, δ , to be an additional free parameter of the optimization. Figure 3 shows the outcome of these free- δ geometry optimizations for an exponential-cylindrical reference nanopore. The RMSE metrics excluded the cylindrical, conical and hyperbolic trial profiles, identical to the behavior seen for the fixed- δ exponential-cylindrical reference nanopores characterization. The fit quality of exponential-cylindrical and conical-cylindrical profiles to the reference conductances, however, could not be distinguished on the basis of the RMSE metrics. In the four-point framework, the optimization of profiles with four free parameters is no longer overdetermined by the available conductance data, and such ambiguity can emerge. A conical profile artificially given four free parameters (r_0 , R , δ and the membrane thickness, L), for example, could also fit the conductance data with similarly low RMSE values. Compared to prior two-point work in which the conductance could not distinguish between a variety of reasonable two-parameter nanopore profiles, however, the current uncertainty is rather benign and can be compensated for by judicious choice of trial profiles,

careful examination of the optimized parameters or additional information²⁷. Best-fit parameters r_0 , l , and b from optimization of the exponential-cylindrical trial profiles exactly matched the reference native pore parameters, and the optimizations also yielded the correct surface coating thickness, δ . The radii of the conical-cylindrical pores were an excellent match to the reference radii, but the inner cylinder lengths, l , could be as much as 8nm larger than the 11 nm reference value. The conical-cylindrical best-fit δ in Figure 3 consistently underestimated the 1.7nm reference value, but not unreasonably so. In general, though, the use of well-defined surface functionalization moieties allows the optimized values of δ to be used as an independent check on the nanopore conductance characterization. The best-fit δ values for the hyperbolic profiles, for example, exceeded the possible length of the monolayer, and can therefore be ruled out or, possibly, could motivate independent additional characterization of the surface decoration.

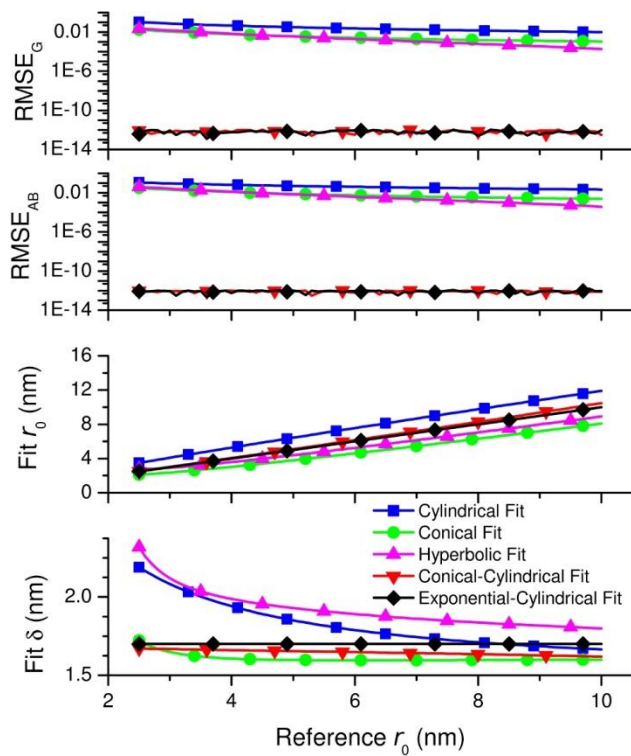


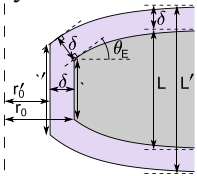
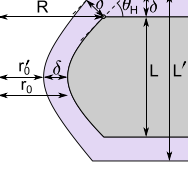
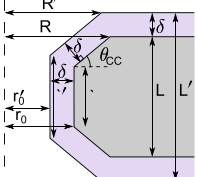
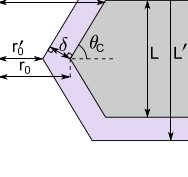
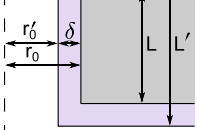
Figure 3. The geometry optimizations of exponential-cylindrical reference nanopores in Figure 2 were repeated, but with δ as a free parameter of the optimization. The top three panels show the metrics and best-fit radii, while the bottom panel shows the corresponding values of the surface coating thickness, δ .

Conclusions

Surface-coated nanopores are receiving increasing attention for the ability of surface coatings to tune nanopore dimensions and surface chemistry, and to confer powerful performance capabilities on a host of nanopore single molecule sensing and manipulation schemes. Knowledge of a nanopore's size, shape and surface chemistry thus bears on nanopore creation, modification and application. While nanopore conductance is governed by the nanopore geometry and surface chemistry in concert with experimental parameters such as electrolyte composition and temperature, careful design is necessary if the measured conductance is to be used to reveal the underlying nanopore properties. The use of experimentally realistic trial nanopore profiles, coupled with consideration of the resulting best-fit parameters in the context of nanopore fabrication and surface functionalization details, is naturally essential to the success of this method. This is especially true when optimizing models with the full four degrees of freedom permitted by the method. The geometry optimization results were achieved using an experimentally-supported nanopore conductance model¹⁰⁻¹¹ that allows the effects of nanopore geometry on the conductance to be clearly separated from the effects of surface chemistry. In this context, the conclusions drawn regarding the quality of the geometry optimization results presented here are general and, so long as the surface modification changes the nanopore dimensions, are not restricted to a particular choice of surface chemical modification.

The four-point conductance framework introduced here was able to correctly identify nanopore shapes and to determine the correct magnitudes of all key geometry descriptors of realistic nanopores with greater structural complexity than had previously been possible by conductance, alone. This capability included the complete characterization of an elegant, experimentally-determined nanopore profile representative of TEM-manufactured nanopores¹⁰ without requiring constraint of its parameters²⁷. The performance capabilities thus dramatically exceed those of the more usual single-point conductance approach based on a cylindrical nanopore approximation, and of the more sophisticated two-point conductance approaches. Beyond recovering the native nanopore structure, the four-point method was able to also probe the thickness of the surface coating, δ . With the use of approaches that yield well-defined surface coatings, the best-fit values for the coating thickness emerge as an additional metric for evaluating the conductance-based nanopore characterization. Straightforward measurements of the electrolyte-concentration-dependent conductance of nanopores can thus serve as a simple yet powerful foothold for peering into these bioinspired nanoscale environments.

Table 1. Listing of nanopore radial profiles with the corresponding transformation of nanopore parameters after coating with a monolayer of thickness δ

<p>Exponential-cylindrical</p> 	<p>Hyperbolic</p> 	<p>Exponential-cylindrical</p> $r'_0 = r_0 - \delta$ $b' = \frac{r_0 - \delta}{2 \tan \theta_E}$ $l' = L + 2\delta - (L - l + 2\delta(1 - \cos \theta_E) + 2\delta(1 - \cos \theta_E)) \exp \left\{ \frac{2\delta \tan \theta_E (1 - \sin \theta_E)}{L - l + 2\delta(1 - \cos \theta_E)} \right\}$ $\tan \theta_E = \frac{L - l}{2} b$	
<p>Conical Cylindrical</p> 	<p>Conical</p> 	<p>Hyperbolic</p> $r'_0 = r_0 - \delta$ $(R')^2 = (r_0 - \delta)^2 + \left(\frac{L + 2\delta}{L + 2\delta \cos \theta_H} \right)^2 [(R - \delta \sin \theta_H)^2 - (r_0 - \delta)^2]$ $\tan \theta_H = \frac{RL/2}{R^2 - r_0^2}$	
<p>Cylindrical</p> 	<p>All</p> $L' = L + 2\delta$ <hr/> <p>Cylindrical</p> $r'_0 = r_0 - \delta$	<p>Conical Cylindrical</p> $r'_0 = r_0 - \delta$ $R' = R + \delta(\cot \theta_{CC} - \csc \theta_{CC})$ $l' = l + 2\delta(\sec \theta_{CC} - \tan \theta_{CC})$ $\tan \theta_{CC} = \frac{(L - l)/2}{R - r_0}$	<p>Conical</p> $r'_0 = r_0 - \delta \csc \theta_C$ $R' = R + \delta(\cot \theta_C - \csc \theta_C)$ $\tan \theta_C = \frac{L/2}{R - r_0}$

Supporting Information. Table S1 listing nanopore radial profiles with the corresponding volume (A) and surface (B) integrals. This material is available free of charge via the Internet at <http://pubs.acs.org>.

AUTHOR INFORMATION

Corresponding Author

*Email: jdwyer@chm.uri.edu.

Author Contributions

The manuscript was written through contributions of all authors. All authors have given approval to the final version of the manuscript.

Funding Sources

This research has been supported by NSF CAREER award CBET-1150085 and by the University of Rhode Island.

Notes

The authors declare no competing financial interest.

ACKNOWLEDGMENT

This research has been supported by NSF CAREER award CBET-1150085 and by the University of Rhode Island.

ABBREVIATIONS

TEM, transmission electron microscope; ref, reference; eff, effective.

REFERENCES

1. Miles, B. N.; Ivanov, A. P.; Wilson, K. A.; Dogan, F.; Japrun, D.; Edel, J. B. *Chem. Soc. Rev.* **2013**, *42*, 15-28.
2. Reiner, J. E.; Balijepalli, A.; Robertson, J. W. F.; Campbell, J.; Suehle, J.; Kasianowicz, J. J. *Chem. Rev.* **2012**, *112*, 6431-6451.
3. Oukhaled, A.; Bacri, L.; Pastoriza-Gallego, M.; Betton, J.-M.; Pelta, J. *ACS Chemical Biology* **2012**, *7*, 1935-1949.

4. Kocer, A.; Tauk, L.; Déjardin, P. *Biosens. Bioelectron.* **2012**, *38*, 1-10.
5. Ma, L.; Cockroft, S. L. *ChemBioChem* **2010**, *11*, 25-34.
6. Tian, Y.; Wen, L.; Hou, X.; Hou, G.; Jiang, L. *ChemPhysChem* **2012**, *13*, 2455-2470.
7. Howorka, S.; Siwy, Z. *Chem. Soc. Rev.* **2009**, *38*, 2360-2384.
8. Bayley, H.; Martin, C. R. *Chem. Rev.* **2000**, *100*, 2575-2594.
9. Davenport, M.; Healy, K.; Pevarnik, M.; Teslich, N.; Cabrini, S.; Morrison, A. P.; Siwy, Z. S.; Létant, S. E. *ACS Nano* **2012**, *6*, 8366-8380.
10. Liebes, Y.; Drozdov, M.; Avital, Y. Y.; Kauffmann, Y.; Rapaport, H.; Kaplan, W. D.; Ashkenasy, N. *Appl. Phys. Lett.* **2010**, *97*, 223105.
11. Smeets, R. M. M.; Keyser, U. F.; Krapf, D.; Wu, M.-Y.; Dekker, N. H.; Dekker, C. *Nano Lett.* **2006**, *6*, 89-95.
12. Aksimentiev, A. *Nanoscale* **2010**, *2*, 468-483.
13. Vlassiouk, I.; Smirnov, S.; Siwy, Z. *Nano Lett.* **2008**, *8*, 1978-1985.
14. Firnkes, M.; Pedone, D.; Knezevic, J.; Döblinger, M.; Rant, U. *Nano Lett.* **2010**, *6*, 895-909.
15. Hoogerheide, D. P.; Garaj, S.; Golovchenko, J. A. *Phys. Rev. Lett.* **2009**, *102*, 256804.
16. Hoogerheide, D. P.; Garaj, S.; Golovchenko, J. A. *Phys. Rev. Lett.* **2010**, *105*, 039902.
17. de la Escosura-Muñiz, A.; Merkoçi, A. *ACS Nano* **2012**, *6*, 7556-7583.

18. Wanunu, M.; Meller, A. *Nano Lett.* **2007**, *7*, 1580-1585.
19. Yusko, E. C.; Johnson, J. M.; Majd, S.; Prangkio, P.; Rollings, R. C.; Li, J.; Yang, J.; Mayer, M. *Nature Nanotechnology* **2011**, *6*, 253-260.
20. Wei, R.; Pedone, D.; Zürner, A.; Döblinger, M.; Rant, U. *Small* **2010**, *6*, 1406-1414.
21. Nam, S.-W.; Rooks, M. J.; Kim, K.-B.; Rossnagel, S. M. *Nano Lett.* **2009**, *9*, 2044-2048.
22. Astier, Y.; Datas, L.; Carney, R.; Stellacci, F.; Gentile, F.; DiFabrizio, E. *Small* **2011**, *7*, 455-459.
23. Tabard-Cossa, V.; Wiggin, M.; Trivedi, D.; Jetha, N. N.; Dwyer, J. R.; Marziali, A. *ACS Nano* **2009**, *3*, 3009-3014.
24. Branton, D.; Deamer, D. W.; Marziali, A.; Bayley, H.; Benner, S. A.; Butler, T.; Di Ventra, M.; Garaj, S.; Hibbs, A.; Huang, X. H.; Jovanovich, S. B.; Krstic, P. S.; Lindsay, S.; Ling, X. S. S.; Mastrangelo, C. H.; Meller, A.; Oliver, J. S.; Pershin, Y. V.; Ramsey, J. M.; Riehn, R.; Soni, G. V.; Tabard-Cossa, V.; Wanunu, M.; Wiggin, M.; Schloss, J. A. *Nat. Biotechnol.* **2008**, *26*, 1146-1153.
25. Kuan, A. T.; Golovchenko, J. A. *Appl. Phys. Lett.* **2012**, *100*, 213104-4.
26. Kim, M. J.; McNally, B.; Murata, K.; Meller, A. *Nanotechnology* **2007**, *18*, 205302.
27. Frament, C. M.; Dwyer, J. R. *The Journal of Physical Chemistry C* **2012**, *116*, 23315-23321.
28. Ayub, M.; Ivanov, A.; Instuli, E.; Cecchini, M.; Chansin, G.; McGilvery, C.; Hong, J.; Baldwin, G.; McComb, D.; Edel, J. B.; Albrecht, T. *Electrochim. Acta* **2010**, *55*, 8237-8243.

29. Vlassiouk, I.; Apel, P. Y.; Dmitriev, S. N.; Healy, K.; Siwy, Z. S. *Proc. Natl. Acad. Sci. U. S. A.* **2009**, *106*, 21039-21044.
30. Wharton, J. E.; Jin, P.; Sexton, L. T.; Horne, L. P.; Sherrill, S. A.; Mino, W. K.; Martin, C. R. *Small* **2007**, *3*, 1424-1430.
31. Kowalczyk, S. W.; Grosberg, A. Y.; Rabin, Y.; Dekker, C. *Nanotechnology* **2011**, *22*, 315101.
32. DeBlois, R. W.; Bean, C. P. *Rev. Sci. Instrum.* **1970**, *41*, 909-916.
33. Behrens, S. H.; Grier, D. G. *J. Chem. Phys.* **2001**, *115*, 6716-6721.
34. van der Heyden, F. H. J.; Stein, D.; Dekker, C. *Phys. Rev. Lett.* **2005**, *95*, 116104.
35. Kasianowicz, J. J.; Bezrukov, S. M. *Biophys. J.* **1995**, *69*, 94-105.

TOC Image

